

# An automatic 3D tomato plant stemwork phenotyping pipeline at internode level based on tree quantitative structural modelling algorithm

Bolai Xin<sup>a,e,\*</sup>, Katarína Smoleňová<sup>b,c</sup>, Harm Bartholomeus<sup>d</sup>, Gert Kootstra<sup>a</sup>

<sup>a</sup> Agricultural Biosystems Engineering, Wageningen University & Research, 6700 AA, The Netherlands

<sup>b</sup> Centre for Crop Systems Analysis, Wageningen University & Research, 6700 AA, The Netherlands

<sup>c</sup> Horticulture and Product Physiology, Wageningen University & Research, 6700 AA, The Netherlands

<sup>d</sup> Laboratory of Geo-Information Science and Remote Sensing, Wageningen University & Research, 6708 PB, The Netherlands

<sup>e</sup> College of Engineering, South China Agricultural University, Guangzhou, China

## ARTICLE INFO

### Keywords:

3D phenotyping  
Point cloud  
Semantic segmentation  
Deep learning  
Tomato plants

## ABSTRACT

Phenotypic traits of stemwork are important indicators of plant growing status, contributing to multiple research domains including yield estimation, breeding engineering, and disease control. Traditional plant phenotyping with human work faces serious bottlenecks on labour intensity and time consumption. In recent years, the application of Quantitative Structural Modeling (QSM) together with three-dimensional (3D) sensor-based data acquisition techniques provides a feasible solution towards the automatic stemwork phenotyping. Nevertheless, existing QSM-based pipelines are sensitive towards the point cloud quality, and mostly focus on the phenotyping at plant or organ level. Information at internode level which are closely related to photosynthesis and light absorption was generally overlooked. To this end, a 3D automatic stemwork phenotyping pipeline is developed for tomato plants at both plant and internode level. Coloured point clouds are taken as the sensor input of the pipeline. A semantic segmentation based on PointNet++ was used to detect and localise the stemwork points. To improve the quality of the segmented stemwork point clouds, a density-based refining pipeline is proposed containing three main processes: non-replacement resampling, interference branch removal, and noise removal. A Tree Quantitative Structural Modeling (TreeQSM) algorithm was then applied to the stemwork point cloud to construct a digital reconstruction. The target phenotypic traits were finally calculated from the digital model by employing an internode association process. The proposed phenotyping pipeline was evaluated with a test dataset containing three tomato plant cultivars: Merlice, Briosio, and Gardener Delight. The related rooted mean squared errors of calculated internode length, internode diameters, leaf branching angle, leaf phyllotactic angle, and stem length range from 4.8 to 64.4%. Considering the time consuming manual phenotyping process, the proposed work provides a feasible solution towards the high throughput plant phenotyping, from which facilitates the related research on plant breeding and crop management.

## 1. Introduction

Plant phenotyping is an acquisition and assessment process of various types of plant traits indicating plant growth, development, architecture, physiology and yield (Li et al., 2014). Phenotyping as a significant domain in bio-engineering plays an important role in modern agricultural research and production (Fahlgren et al., 2015). Since the plant phenotype is formed during plant growth, as a result of the interaction between genotype and environment (Li et al., 2020), plant phenotyping techniques provide an efficient way to the comprehension of interactions among the three of them (Paul et al., 2019; Diouf et al., 2020).

By connecting genotype to phenotype, high yielding, stress-tolerant plants can be selected in a rapid and efficient way (Li et al., 2014), which then eases relevant research on genetic improvement through breeding engineering (Phillips, 2010). Furthermore, plant phenotyping techniques enable the identification and the quantification of plant diseases at early time points in epidemics, which makes the early and accurate diagnosis available to reduce the quality and quantity losses in crop yield (Mahlein, 2016).

Traditional plant phenotyping mainly relies on manual observations and measurements (Gehan and Kellogg, 2017), which are exceptionally

\* Corresponding author at: Agricultural Biosystems Engineering, Wageningen University & Research, 6700 AA, The Netherlands.

E-mail addresses: [b.xin@scau.edu.cn](mailto:b.xin@scau.edu.cn) (B. Xin), [katarina.smolenova@wur.nl](mailto:katarina.smolenova@wur.nl) (K. Smoleňová), [harm.bartholomeus@wur.nl](mailto:harm.bartholomeus@wur.nl) (H. Bartholomeus), [gert.kootstra@wur.nl](mailto:gert.kootstra@wur.nl) (G. Kootstra).

<https://doi.org/10.1016/j.compag.2024.109607>

Received 6 December 2023; Received in revised form 8 August 2024; Accepted 28 October 2024

Available online 9 November 2024

0168-1699/© 2024 The Authors. Published by Elsevier B.V. This is an open access article under the CC BY license (<http://creativecommons.org/licenses/by/4.0/>).

## Nomenclature

$\eta$	Proportional threshold used to remove the interference branch candidates
$P_o$	Original point cloud of a tomato plant
$P_s^j$	Sub point cloud of a tomato plant at the $j$ th down sampling step
$\xi$	The adjustment factor used to select the seed points of cover sets
$D_q$	The minimum distance among seed points during the cover set generation
$D_a^m$	Chi-square distance between the distributions of phenotypic traits calculated from the automatic stemwork segmentation and the manual segmentation
$D_{gt}^a$	Chi-square distance between the distributions of phenotypic traits calculated from the automatic stemwork segmentation and the corresponding ground truth
$D_{gt}^m$	Chi-square distance between the distributions of phenotypic traits calculated from the manual stemwork segmentation and the corresponding ground truth
$E_m$	Mean absolute error
$E_r$	Related rooted mean squared error
$F1$	F1 score
$l_r$	Initial learning rate
$N_e$	Number of epoches
$N_l$	Number of leaves to be exchanged during the crossover augmentation
$N_o$	Number of points within the original point cloud of a tomato plant
$N_p$	The number of points within the input point clouds of the segmentation network
$N_\epsilon^1$	Threshold of horizontal point density used to remove the stem points
$N_\epsilon^2$	Threshold of local point density used to determine the inner points during the DBSCAN clustering
$N_{min}^1$	Minimum number of points to accept a cover set seed proposal during the morphology analysis step
$N_{min}^2$	Minimum number of points to accept a cover set seed proposal during the sub-cylinder reconstruction step
$P_r$	Precision
$R_e$	Recall
$R_q$	Radius of query ball for the cover set generation

labour intensive and time consuming (Furbank and Tester, 2011). Unavoidable subjective biases also commonly exist within the data collected by different collectors. In addition, manual phenotyping is sometimes conducted in a destructive form, which makes the continuous tracking and measuring of phenotypic traits within time series impossible (Fahlgren et al., 2015).

As the rapid development of sensing techniques in recent decades, sensor-based phenotyping provides a feasible solution towards the above problems (Andrade-Sanchez et al., 2013; Bai et al., 2016; Laxman et al., 2018; Cardellicchio et al., 2023; Sheikh et al., 2024). Among

various types of sensor-based data, point cloud data enables a versatile acquisition of plant geometry information in 3D space, and is consequently becoming pivotal for quantifying plant traits. Comparing with traditional 2D plant phenotyping, 3D point cloud data efficiently solves the problems of ambiguity of plant size caused by camera viewpoints, lack of 3D information regarding plant volume and leaf area, and self occlusion caused by the complex plant structure (Zhang et al., 2018; Wang et al., 2022). To acquire the phenotypic traits from a point cloud, a segmentation process is usually required to localise the plant organ of interest. For example, Hang et al. (2017) applied horizontal density-based approach to segment the main stem from other plant organs; Ziamtsova and Navlakha (2019) calculated various types of point features including Point Feature Histograms (PFH), Fast Point Feature Histograms (FPFH), and radius-based surface descriptor, and segmented a tomato plant into leaflets and stem using machine learning algorithms; Wu et al. (2019) and Xiang et al. (2019) introduced skeletonisation algorithm to localise the main stem of maize and sorghum plants. Nevertheless, these kinds of segmentation algorithms highly rely on human work to stipulate discriminative feature types, which largely limits their applications considering the natural variations. Modern research introduced deep neural networks in the study of 3D semantic segmentation of plant organs. For example, Heiwolt et al. (2021) achieved the semantic segmentation of plant organs by taking PointNet++ as the backbone; Boogaard et al. (2022) further proposed a class-dependent sampling approach over the traditional PointNet++ to overcome the problem of unbalanced dataset. Due to the automatic feature learning function, deep-learning-based point cloud segmentation has shown a more robust performance compared to the approaches using manual feature extraction. However, deep-learning-based segmentation generally requires a large training dataset to prevent overfitting, where the annotation processing of 3D point clouds was exceptionally time consuming and labour intensive.

To measure phenotypic traits of interest from the segmented point clouds, existing work has employed multiple geometry-based approaches to achieve the calculations of various plant traits. For example, Boogaard et al. (2023) measured internode lengths of cucumber plants from dual-view-point point clouds with PointNet-based node detection, resulting in a Mean Average Errors (MAE) of 5.0 mm; Rose et al. (2015) and Bao et al. (2019) performed stem height measurements of tomato and maize plants respectively, indicating MAEs ranging from 1.39–15 mm; Rose et al. (2015), Li et al. (2017), and Itakura and Hosoi (2018) achieved leaf area estimation using voxel counting and surface mesh reconstruction, indicating related rooted mean squared errors ranging from 1.4–17.4%; Bao et al. (2019) and Zhu et al. (2023) conducted leaf angle measurements from the skeletonised stemwork point clouds, achieving MAEs of 3.5 and 5.2° respectively; Schunck et al. (2021) calculated leaf lengths of maize and tomato plants using Poisson surface reconstruction algorithm, achieving a MAE of 8.9 mm. Furthermore, Raunonen et al. (2013) and Du et al. (2019) proposed a Quantitative Structural Modeling (QSM) approach to fit a comprehensive digital model of the stemwork, from which quantified a number of general phenotypic traits of plant stemwork. To achieve this, morphological analysis and skeletonisation process were employed to track individual branches within the point cloud. The shape of branches was then described using multiple end-to-end sub-cylinders. QSM approaches enable high-throughput phenotyping of tree structures by taking versatile geometry traits into consideration, such as branch angles, surface areas, and volumes. Nevertheless, QSM algorithms introduce sub-cylinders to fit the stemwork structures of plants, where information at internode level is not available. Knowing that traits of internodes are closely related to photosynthesis and light absorption (Sarlikioti et al., 2011a,b), there has been a great importance to perform the phenotyping at internode level. Apart from this, the most significant drawback of traditional QSM-based phenotyping is the sensitivity towards the quality of stemwork point cloud. A point cloud with low signal-noise ratio and resolution may give rise to a large error when performing the digital model fitting with QSM algorithms, or even lead to a failed model generation.

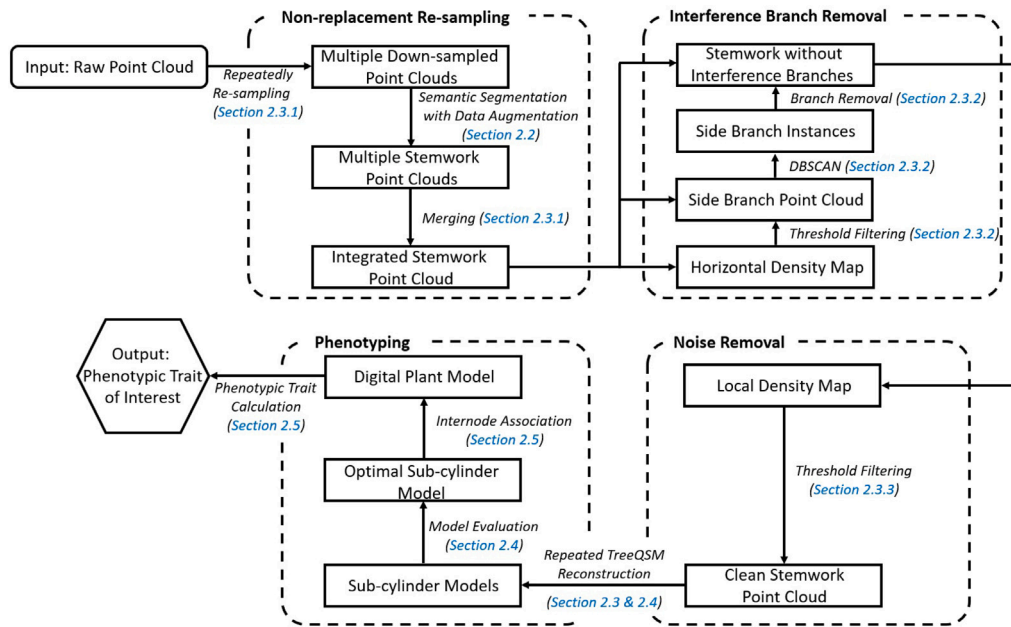


**Fig. 1.** A flowchart of the complete phenotyping pipeline. Here, data objects are presented as the normal font inside the rectangular blocks. Data flow orientations are presented by arrows. Data processes are presented with an italic font.



**Fig. 2.** Morphology of selected tomato plant cultivars: (a) Merlice, (b) Brioso, and (c) Gardener Delight.

To perform a reliable plant phenotyping with QSM-based pipeline, especially over the point clouds with relatively lower quality, the primary objective of this article is to develop a novel refining pipeline to enhance the quality of segmented stemwork point clouds. The refining pipeline consists of three main process, i.e. non-replacement resampling, interference branch removal, and noise removal. To enhance the function of QSM-based phenotyping pipeline, especially in aspect of the acquisition of internode traits, the second objective is to perform a comprehensive digital plant reconstruction and morphological analysis over the refined stemwork point cloud by taking TreeQSM as the backbone. Target phenotypic traits include stem internode length, stem internode diameter, branching angle, phyllotactic angle, and stem length.

## 2. Materials and methods

To detect and localise the stemwork from a point cloud, a semantic segmentation was performed using a deep neural network (Section 2.2). In order to meet the basic requirement of the following phenotyping process, a refining pipeline was proposed for the stemwork segmentation, including three main process: non-replacement resampling

(Section 2.3.1), interference branch removal (Section 2.3.2), and noise removal (Section 2.3.3). A local reconstruction (Section 2.3) was then performed to the segmented stemwork point cloud with a parameter optimisation process (Section 2.4). The target phenotypic traits were finally calculated with an internode association process (Section 2.5). The experimental details are provided in Section 2.6, followed by an introduction of the evaluation metrics in Section 2.7. For a better understanding, a flowchart of the complete phenotyping pipeline is shown in Fig. 1.

### 2.1. Dataset acquisition

Three commonly used tomato (*Solanum lycopersicum* L.) cultivars with different morphology were selected to test the transferability of the proposed phenotyping pipeline: 17 Merlice plants, 20 Brioso and 8 Gardener Delight. Here, Merlice and Brioso generally indicate small leaf curvature and large branching angles, resulting in a loose canopy structure; while Gardener Delight commonly possesses sagging leaves with large curvature, resulting in relatively dense leave structure, as shown in Fig. 2.

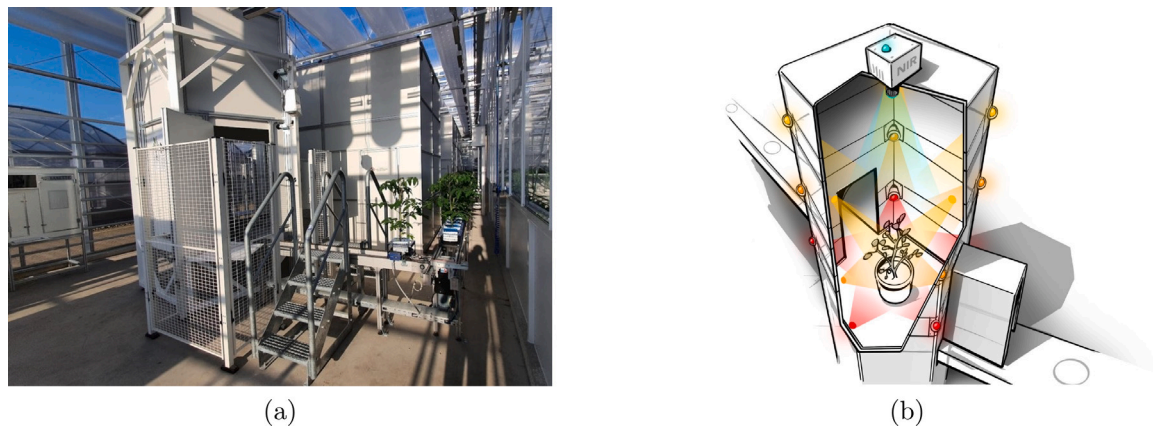


Fig. 3. The imaging system - Maxi-Marvin - being used to acquire individual plant point cloud data. (a) shows the outline of the imaging unit; (b) shows a schematic drawing of the camera setup inside the imaging black box.

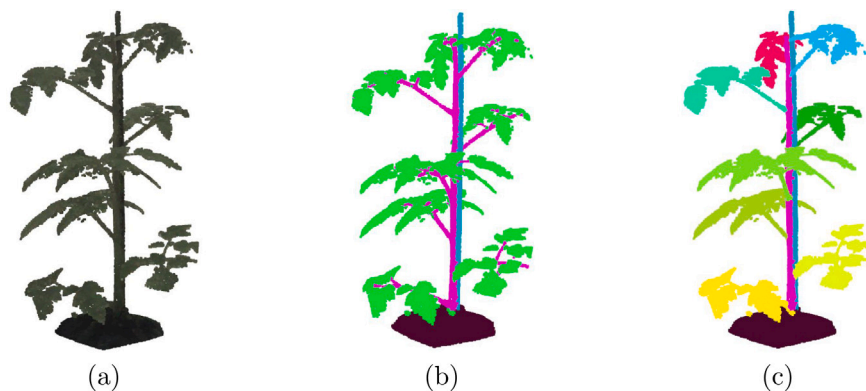


Fig. 4. Examples of tomato plant point cloud being used in the proposed work. (a) shows an original RGB point cloud of tomato plant; (b) shows the corresponding semantic labels, where pink refers to the stemwork, green refers to leaflets, light blue refers to the supporting stick, and brown refers to the soil base; (c) shows the corresponding instance labels.

A well-developed imaging device - Maxi-Marvin - was used to scan the plants. The setup for the Maxi-Marvin is shown in Fig. 3. Fifteen RGB cameras with a resolution of  $1920 \times 1080$  were mounted around the plant within a pentaprism-shape imaging black box, on three different heights and five different angles. The RGB cameras gave fifteen images of the target plant simultaneously during each exposure. The point clouds of target plants were reconstructed using the shape-from-silhouette method (Golbach et al., 2016). A 3D voxel space setting at the centre of the imaging facility with a size of  $40 \text{ cm} \times 40 \text{ cm} \times 70 \text{ cm}$  in length, width and height respectively and a resolution of  $1 \text{ mm}^3$  was used during the reconstruction. Each point cloud acquired with the Maxi-Marvin contains 48 channels, where the first three channels are 3D positions of points, followed by 45 channels of colour information of points (red, green and blue for each camera image). Fig. 4(a) shows an example of the coloured point cloud captured by the imaging setup. More details on the point cloud reconstruction from images based on the shape-from-silhouette algorithm are introduced in Golbach et al. (2016). The scanning process was conducted during the second and third weeks after sowing, where 19 plants (7 Merlice, 8 Brioso, and 4 Gardener Delight) were scanned in the second week and 26 plants (10 Merlice, 12 Brioso, and 4 Gardener Delight) were scanned in the third week. The overall dataset was split into a training set ( $T_p$ ), a validation set ( $V$ ), and a test set ( $T_e$ ), which contain 35, 5, and 10 point clouds respectively.

#### 2.1.1. Point cloud annotation

During the manual annotation process, each point within a point cloud was given a semantic label and an instance label. Semantic

labelling divided points into four classes: soil, stick, stemwork, and other bio-structures, as shown in Fig. 4(b). Here, the stemwork refers to the collection of the main stem, petioles,<sup>1</sup> rachis<sup>2</sup> and petiolules.<sup>3</sup> Other bio-structures refer to the collection of leaflets and trusses.<sup>4</sup> The terminology of plant organs employed in this paper follows the work presented by Altartouri et al. (2015). Specifically in this paper, the stemwork structure within a leaf candidate is called a side branch. The collection of the main stem and all the side branch candidates forms the stemwork of a plant.

Since the proposed work introduced data augmentation methods which required operations at the leaf level, instance labelling was also conducted to facilitate the localisation of each leaf instance. Instance labelling divided a point cloud into classes of soil, stick, the main stem, and all leaf instances, as shown in Fig. 4(c). Here, a leaf instance refers to the collection of the petiole, rachis, petiolules and leaflets.

#### 2.1.2. Destructive measurements

Destructive measurements of the selected plants were conducted right after the imaging process. Stem internode length, stem internode diameter, leaf branching angle, leaf phyllotactic angle, and total stem length were taken as the objective phenotypic traits and measured

<sup>1</sup> A petiole refers to the first secondary internode on a leaf, which is directly connected to the main stem.

<sup>2</sup> Rachis refers to the secondary internodes on a leaf following after the petiole.

<sup>3</sup> Petiolules refer to the tertiary internodes in a tomato plant.

<sup>4</sup> A truss refers to the small side branch with flowers and fruits on it.



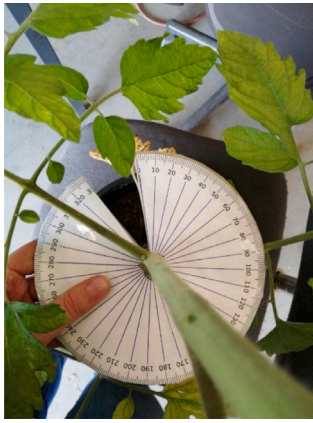


Fig. 5. The protractor with a caliper specifically designed to measure the phyllotactic angle of leaves.

manually. Internode length and stem length were measured with a ruler with an accuracy of 1 mm. Internode diameter was measured with a caliper with an accuracy of 0.1 mm. Branching angle refers to the inclination angle of a leaf to the parent stem internode, which was measured with a traditional protractor with an accuracy of 1 degree. Phyllotactic angle refers to the clockwise angle between the petiole of two consecutive leaves. To measure the leaf phyllotactic angle, a specific protractor with a caliper was designed with an accuracy of 1 degree, as shown in Fig. 5. During the measurement, the protractor was mounted onto the main stem of the target plant through the circular caliper in the middle. The origin line was aligned with the petiole orientation of the leaf with a lower morphological rank. The phyllotactic angle was then indicated by the value displayed by petiole orientation of the leaf with a higher morphological rank. Morphological ranks are counted by the nodes on the stem. The bottom node on the stem refers to the first morphological rank of a plant, and all following nodes until the morphological top of the plant. The shape of stem internodes are indicated as elliptical cylinders. This gives rise to different values of diameter measurements of a stem internode from different orientations. In this work, the internode diameter was taken as the average value of two orthogonal measurements conducted at the middle point of an internode.

## 2.2. Semantic segmentation

To identify and localise the stemwork within a tomato plant point cloud, semantic segmentation was conducted according to the types of plant parts. One of the top-performing point cloud semantic segmentation network - PointNet++ was employed as the backbone (Guo et al., 2020). The original version of PointNet series - PointNet Vanilla (Qi et al., 2017a) uses shared multiple layer perceptron to capture the feature vectors of individual points. To satisfy the requirements of permutation invariance, a max or average pooling layer is employed over the acquired feature vectors in order to obtain a global feature description of the point cloud. To take the hierarchical feature context into consideration, an improved version - PointNet++ was proposed by further introducing set abstraction layers and feature propagation layers (Qi et al., 2017b). A set abstraction layer is composed by a sampling and grouping process followed by a PointNet feature extractor. The sampling and grouping process aims to divide the original point cloud into multiple clusters. The PointNet feature extractor applied to individual point clusters achieves a multi-scale learning of local point features. Feature propagation layers then use interpolation operations to propagate the multi-scale features back to each point in

the point cloud. Combined with the fully connection layers, PointNet series achieve a reliable performance on point cloud segmentation and classification.

To deal with the overfitting problem caused by insufficient training data, a 3D local data augmentation approach - leaf crossover - proposed in our preceding work (Xin et al., 2023) was used to enhance the dataset diversity. Leaf crossover augmentation aims to exchange the leaf instances among different plants after the acquisition of each training batch. To maintain the unique attributes with respect to plant cultivar and morphological ranks,<sup>5</sup> the crossover operation only exchanges the leaf instances within the same cultivar and with the same morphological rank. The position and the phyllotactic angle of the leaf candidate to be exchanged are aligned to the original leaf instance on the target plant. The overall process of leaf crossover augmentation is visualised in Fig. 6. More details on leaf crossover augmentation are introduced in Xin et al. (2023) Section 2.3.2.

A random down sampling was performed to the point clouds after the data augmentation process in order to uniform the shape of point clouds within a training batch, as required by the PointNet++ configuration. Considering the limitations of GPU memory, the number of points of each point cloud was finally set to 50,000 in this paper. The input features contain point positional information (channel 1 to 3), point normal information (channel 4 to 6), and point colour information (channel 7 to 51), which then forms an input point cloud with the shape of  $50\,000 \times 51$ . Batch size was set to five throughout the experiment to save the GPU memory. A 7-fold cross validation over the training set was used to select the hyper parameters for the network. Here, hyper parameters included initial learning rate  $l_r$ , epoch number  $N_e$ , and number of leaf instances  $N_l$  to be exchanged per plant during the leaf crossover augmentation. The combination with the highest stemwork segmentation  $F1$  score was selected, resulting in  $l_r = 0.005$ ,  $N_e = 150$ , and  $N_l = 4$  respectively.

## 2.3. Stemwork local reconstruction

To further approach the phenotypic traits of interest, an important step is to reconstruct the stemwork point cloud into a digital model. One of the commonly used algorithms - Tree Quantitative Structural Modeling (TreeQSM)<sup>6</sup> (Raumonen et al., 2013) - was employed to achieve the reconstruction. TreeQSM is a high-throughput 3D phenotyping pipeline specifically developed for tree structures integrating functions of morphology analysis, model fitting, and model trait calculation. TreeQSM is built upon the cover set theory. The stemwork point cloud is randomly partitioned into multiple cover sets, where each cover set is known as the minimum unit to perform the stemwork reconstruction. A cover set is generated according to the following two steps. In the first step, a query ball with a radius of  $R_q$  is applied to an automatically and randomly selected seed point to propose a potential cover set centre. Here, the selection of a seed point should satisfy the condition that the minimum distance between two arbitrary existing seed points is larger than a threshold  $D_q$ . The threshold  $D_q$  is usually slightly smaller than the radius of query balls ( $D_q = R_q - \xi$ ) to ensure a better coverage of cover sets over the stemwork point cloud. The cover set centre proposal is accepted if the number of neighbouring points within the query ball is larger than a threshold  $N_{min}$ . The first step is repeated until all the points in the stemwork point cloud are allocated within at least one cover set. In the second step, points within the stemwork point cloud are allocated to each cover set according to the distance to the nearest accepted cover set centre. More details on the definition of cover set are provided in Raumonen et al. (2013).

<sup>5</sup> The leaf shape, branching angle, and phyllotactic angle maintain differences among different tomato plant cultivars and morphological ranks.

<sup>6</sup> The latest release of TreeQSM pipeline - version 2.4.1: <https://github.com/InverseTampere/TreeQSM>.

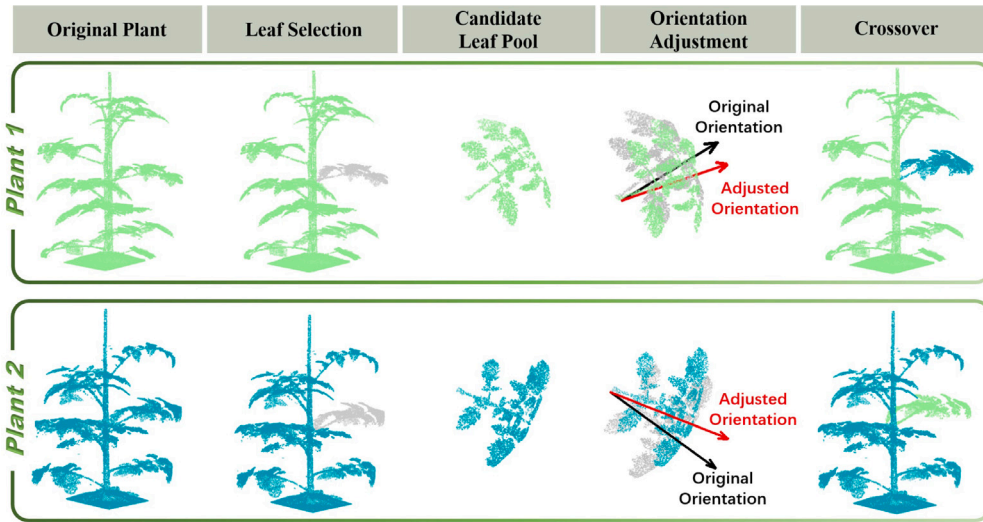


Fig. 6. Legend of leaf crossover augmentation.

Given a stemwork point cloud, TreeQSM performs a neighbour-related morphology analysis at cover set level to segment the points into the main stem, individual secondary branches<sup>7</sup> and individual tertiary branches,<sup>8</sup> as shown in Fig. 7(a). Here, the parameters used to define the cover sets are noted as  $R_q^1$ ,  $\xi^1$ , and  $N_{min}^1$ . The points within each branch with a same branch order,<sup>9</sup> or the points within the main stem are defined as a segment. To illustrate this further, Fig. 7(b) visualises all the detected segments with different colours. The morphology analysis also automatically detects the start point of each segment, which serves as input for the following reconstruction step.

To further visit the plant traits of interest, a cylinder least square based fitting is performed to each detected segment starting from the detected starting point until the terminus. To accurately describe the local shape of the segment, the cylinder fitting is performed at cover set level, where each cover set results in a sub-cylinder object describing the shape at the local region. Parameters used to define the cover set are noted as  $R_q^2$ ,  $\xi^2$ , and  $N_{min}^2$ . Different from the cover set using a fixed query ball radius in the morphology analysis, cover set here employs varying radius drawing within the range  $[R_q^2(min), R_q^2(max)]$ . Here,  $R_q^2(max)$  refers to the query ball radius at the base of each segment, while  $R_q^2(min)$  refers to the query ball radius at the tip of each segment. The variations in query ball radii enable a better capture of local shape features, particularly at the tip of each segment. The whole stemwork point cloud is finally reconstructed with multiple sub-cylinders, as shown in Fig. 7(c).

To ensure the reconstruction performance, three basic assumptions about the input stemwork point cloud must be satisfied:

- A1. The surface of plant structure must be covered by sufficient points<sup>10</sup>;
- A2. The base point of the stem (the bottom of the stem) must be clearly visible without occlusions by other organs, and the base

point of side branches must be higher than the base point of the stem;

- A3. Points other than the stemwork must be properly removed.

Considering the potential deficiencies existing in the stemwork point clouds segmented with PointNet++, we accordingly proposed a refining pipeline to improve the quality of the stemwork point clouds. The refining pipeline is composed by three main process: non-replacement resampling, interference branch removal, and noise removal.

### 2.3.1. Non-replacement resampling

The segmented stemwork point clouds generally indicated low point densities due to the down sampling operation required by the semantic segmentation network<sup>11</sup> (Section 2.2). To improve the density of the stemwork point clouds, a non-replacement resampling process was introduced in order to satisfy assumption A1. To perform the resampling operation from the original point cloud  $P_o$ , the order of points within  $P_o$  was randomly shuffled. At the  $j$ th down sampling step, a sub point cloud  $P_s^j$  was formed by selecting point candidates from  $P_o$  with indices ranging from  $(j-1) * N_p + 1$  to  $j * N_p$ . Here,  $N_p$  is the input point number of the segmentation network (in this paper,  $N_p = 50,000$ ). The semantic segmentation method introduced in Section 2.2 was applied to each down-sampled point cloud  $P_s^j$ . The resampling and segmentation process were repeated for  $\text{floor}(N_o/N_p)$  times, and the stemwork points determined by each resampling and segmentation process were integrated to form a final stemwork point cloud. Here,  $N_o$  is the number of points within the original point cloud  $P_o$ . For a better understanding, the resampling process is further demonstrated in Fig. 8.

### 2.3.2. Interference branch removal

The TreeQSM algorithm automatically detects the base point of the stem, and takes it as the origin of the digital model (Raumonen et al., 2013). This process must be conducted under the circumstance that Assumption A2 has been satisfied.<sup>12</sup> Otherwise, it may give rise

<sup>7</sup> A secondary branch refers to the collection of the petiole which is directly connected to the main stem, and all the following rachis.

<sup>8</sup> A tertiary branch refers to the collection of all the petiolules that generated from a node on the secondary branch.

<sup>9</sup> Branch order zero refers to the main stem. All the secondary branches share the branch order one. All the tertiary branches share the branch order two.

<sup>10</sup> To evaluate whether the surface of plant structure is covered by sufficient points, the following factors are taken into consideration: the resolution of the point cloud, the signal-noise ratio of the point cloud, the complexity of the object structure, and the size of the object.

<sup>11</sup> The tomato plant point clouds being used in the proposed work contained 422,682 points on average. However, the capacity of the semantic segmentation network was trained on 50,000 points per plant only. Therefore, the densities of points within the down-sampled point clouds were much lower than the original.

<sup>12</sup> In reality, Assumption A2 cannot be satisfied in most occasions. For example in Fig. 9(a), the base point of the main stem is higher than the base point of the lowest side branch, which makes it difficult for the stem base detection algorithm to figure out the real base point.

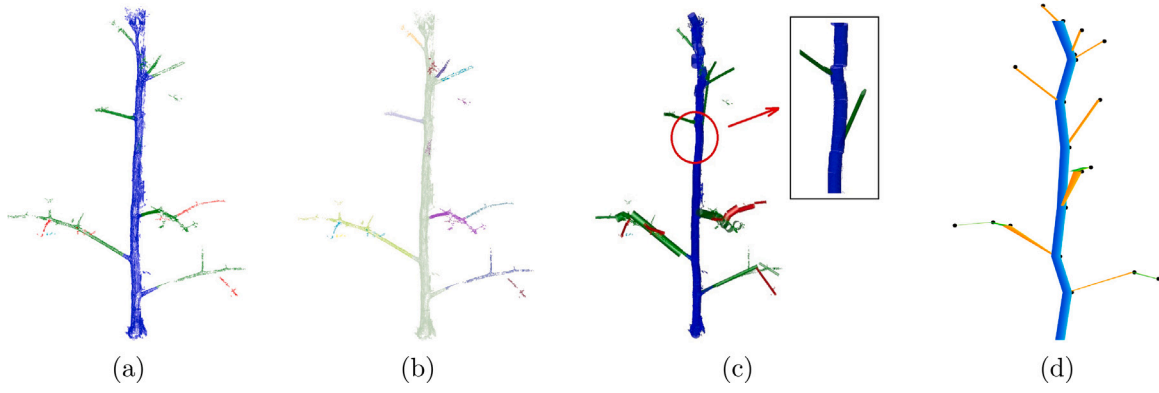


Fig. 7. An example of the digital reconstruction process. (a) shows the morphological analysis result; (b) shows individual detected segments being considered during the local reconstruction process; (c) shows the sub-cylinder fitting process; (d) shows the final digital model of the stemwork.

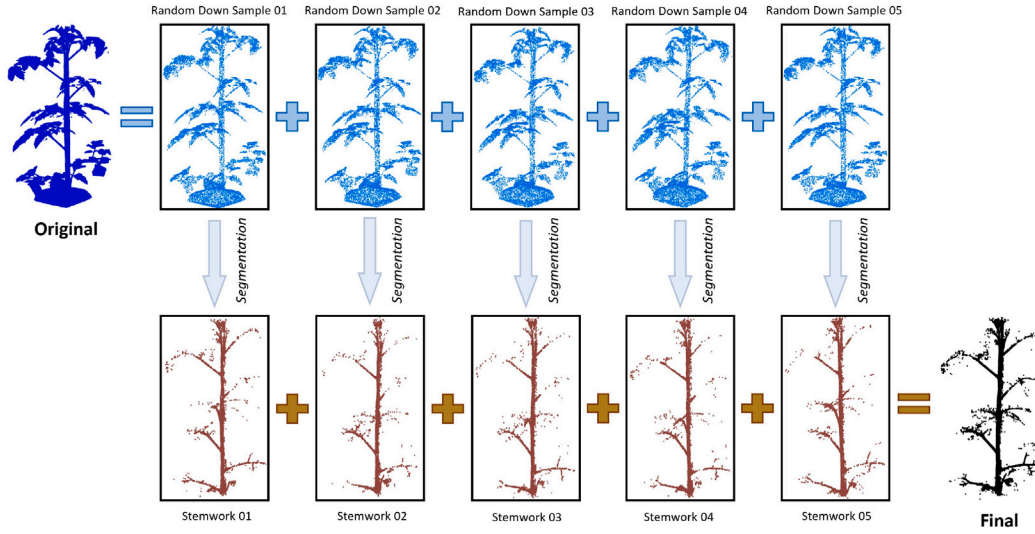


Fig. 8. Illustration of the resampling process. The original point cloud contains 283,530 points, which results in a five-fold resampling process according to the description in Section 2.3.1. The final integrated stemwork point cloud demonstrates a much better point density compared to a single down sampling and segmentation process.

to a false stem base detection result, leading to a plant model with significant deformations, particularly for the stem internodes close to the bottom.

To deal with the side branches at the bottom of the plants that may influence the detection of the stem base, an interference branch removal algorithm was developed through the following four steps:

- Step 1: Stem point removal. Inspired by Hang et al. (2017), a stem point removal algorithm was developed based on horizontal point density map. All the points within the stemwork point cloud are projected onto the horizontal plane  $XOY$ . The local density of each point candidate was then calculated from the projection by using a query ball. Here, the radius of the query ball is a hyper parameter denoted as  $\epsilon_1$ . The local density is given as the number of neighbouring points within the query ball. Fig. 9(b) shows an example of horizontal local point density map obtained from the stemwork point cloud shown in Fig. 9(a), where a colour closer to white refers to a higher local density. It is clearly observed that the projections of stem points generally indicate a higher density than that of the side branches. To remove the stem points, a simple thresholding method was used to select those points whose local density was smaller than the given threshold  $N_\epsilon^1$ . The result of stem point removal is shown in Fig. 9(c).
- Step 2: Branch instance segmentation. Side branch instances within the stemwork point cloud after stem point removal process

are clearly separated from each other. To further visit individual side branches, an instance segmentation of branches was conducted based on the algorithm of Density-Based Spatial Clustering of Applications with Noise (DBSCAN). Starting from a randomly selected seed point, inner points were iteratively searched using a query ball with the radius denoted as  $\epsilon_2$ . Points with local density higher than the given threshold  $N_\epsilon^2$  were considered as the inner points, and grouped into the same cluster. If there was no inner point being detected with respect to a seed point, the seed point was considered as a noise point which was not considered in the final clustering result. This grouping process was repeated multiple times until all the candidate points were clustered into groups. An instance segmentation result of side branches is shown in Fig. 9(d).

- Step 3: Interference branch removal. To identify the branches that may interfere with the stem base detection, the centroid  $C = [x_c, y_c, z_c]$  of the bottom 10% of points within each side branch instance was calculated. If  $z_c < p_b^z + \eta(p_u^z - p_b^z)$ , then the side branch candidate was considered as a potential interference branch to be removed. Here,  $p_b^z$  refers to the  $Z$  coordinate of the bottom point within the stemwork point cloud,  $p_u^z$  refers to the  $Z$  coordinate of the top point, and  $\eta$  is a hyper parameter referring to the proportional threshold. A result of interference branch removal is shown in Fig. 9(e).



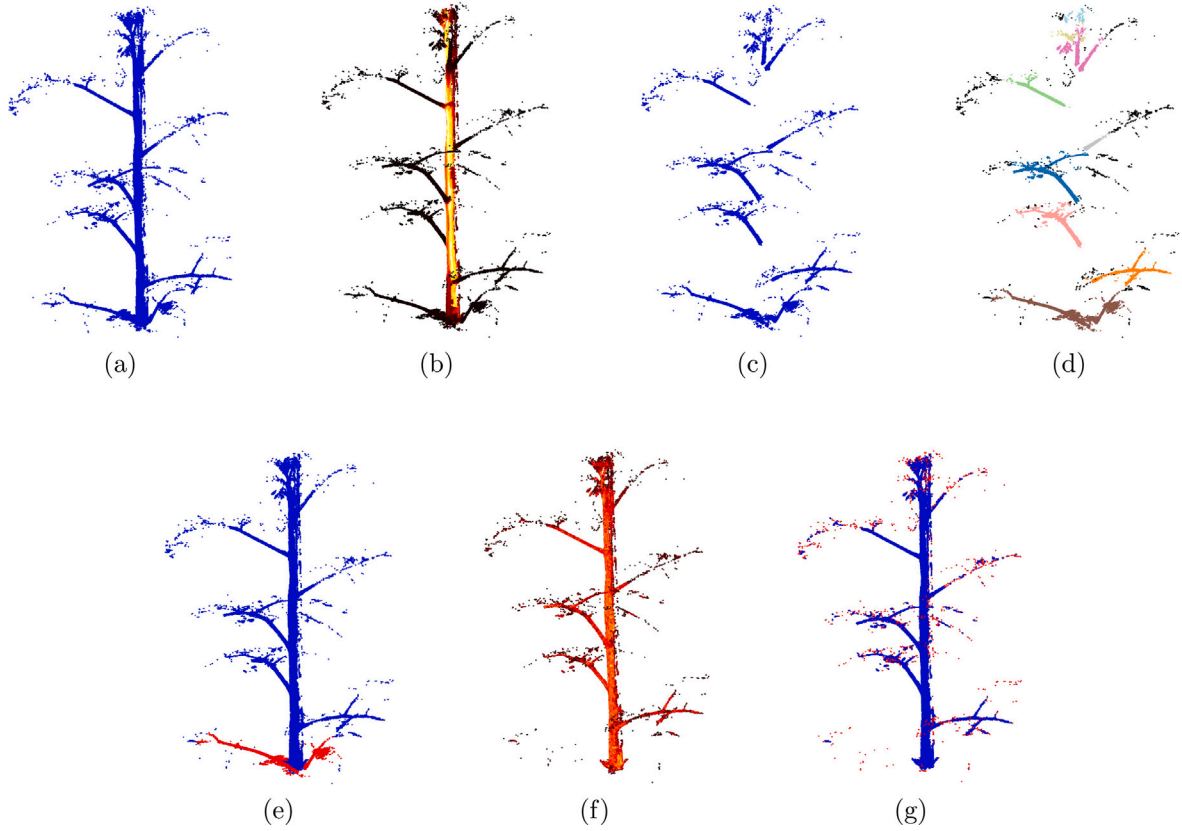


**Fig. 9.** A demonstration of interference branch removal and noise removal. (a) shows an integrated stemwork point cloud acquired from the resampling process introduced in Section 2.3.1. (b) to (e) show the process of interference side branch removal, in which (b) shows the horizontal density map; (c) shows the result of stem removal; (d) shows the instance segmentation result of side branches; and (e) shows the identification result of the potential interference side branches (marked in red), which will be removed from the stemwork point cloud. (f) and (g) show the noise removal process, where (f) shows the 3D local density map, and (g) shows the identified noise points (marked in red) over the remained stemwork points (marked in blue).

### 2.3.3. Noise removal

To further remove the noise points within the stemwork point cloud, a local-density-based noise removal method was employed. The 3D local density of each candidate point was calculated using a query ball whose radius is denoted as  $\epsilon_3$ . Fig. 9(f) reveals an example of 3D local density map calculated from Fig. 9(e). Points with a low local density are then considered to be noise, which can be removed with a simple thresholding method. The threshold used here is a hyper parameter denoted as  $N_\epsilon^3$ . A result of the noise removal process is shown in Fig. 9(g).

## 2.4. Optimal model selection

The sub-cylinder reconstruction process based on TreeQSM algorithm requires multiple presetting parameters, as introduced in Section 2.3. The selection of these parameters largely influence the reconstruction performance. To optimise the parameter selections, several feasible values were proposed for each parameter according to the attributes of training data.<sup>13</sup> With respect to the tomato plant dataset used in this paper, an initial proposal of TreeQSM parameters is shown in Table 1. To create a valid input tuple for the TreeQSM algorithm, one feasible value was drawn from each parameter box to form a

combination including seven elements. With respect to the feasible value proposal revealed in Table 1, totally 900 ( $3 \times 1 \times 5 \times 4 \times 1 \times 3 \times 5$ ) different combinations of potential input parameters were generated. Considering the randomness within the TreeQSM reconstruction process, ten sub-cylinder models were fitted with respect to each valid input parameter tuple, resulting in 9000 sub-cylinder models in total for a single target plant.

The optimal model was selected according to a specified metric, based on the two types of optimal model selection criteria provided by the TreeQSM algorithm, known as cylinder distance and surface coverage. Cylinder distance evaluates the average distance between each candidate points towards the centre axis of the fitted sub-cylinder. A shorter average cylinder distance refers to a better fitting performance. Surface coverage measures the proportion of reconstructed sub-cylinder surface that is covered by sufficient point candidates. A sub-cylinder model with a poor surface coverage means that a large bias exists between the reconstructed cylinder attributes towards the actual point candidates. More details of the above model selection metrics are provided in Raunonen (2015).

A validation step was used to determine the optimal selection metric for the model selection. Point clouds within the validation set  $\mathbb{V}$  were processed with the semantic segmentation and the refining pipeline introduced in Sections 2.2 and 2.3 respectively. The resulting clean stemwork point clouds were then taken as the input for TreeQSM. Sub-cylinder models were fitted by using all the valid input parameter setups. The optimal models were selected using the cylinder distance and surface coverage metrics respectively. The selected optimal models were evaluated with a topology evaluation metric – *F1* score – as introduced in Section 2.7. The model selection metric with a higher topology *F1* score of the selected model was finally selected. In the

<sup>13</sup> The attributes of training data related to the selection of TreeQSM hyper parameters include: average local point density (related to the selection of  $N_{min}^1$  and  $N_{min}^2$ ), maximum and minimum lengths of stem internodes (related to the selection of  $R_q^2(max)$ ,  $R_q^2(min)$ , and  $\xi^2$ ), maximum and minimum stem base diameters (related to the initialisation of  $R_q^1$  and  $\xi^1$ ), and average branch tip diameter (related to the selection of  $R_q^2(min)$  and  $\xi^2$ ).



**Table 1**

Feasible value proposals of necessary parameters required in the TreeQSM algorithm, specifically proposed for the tomato plant dataset used in this paper.

Parameters	Descriptions	Feasible values
$R_q^1$	Radius of query balls used to create the cover set in the morphology analysis step (unit: mm)	25, 35, 45
$\xi_q^1$	Adjustment factor of the minimum distance among cover set seeds in the morphology analysis step (unit: mm)	3
$N_{min}^1$	Threshold of minimum number of points to accept a cover set seed proposal in the morphology analysis step	3, 6, 10, 15, 20
$R_q^2(min)$	Minimum radius of query balls used to create the cover set in the sub-cylinder reconstruction step (unit: mm)	2, 3, 4, 5
$R_q^2(max)$	Maximum radius of query balls used to create the cover set in the sub-cylinder reconstruction step (unit: mm)	15
$\xi_q^2$	Adjustment factor of the minimum distance among cover set seeds in the sub-cylinder reconstruction step (unit: mm)	1, 2, 3
$N_{min}^2$	Threshold of minimum number of points to accept the cover set seed proposal in the sub-cylinder reconstruction step	1, 3, 6, 10, 20

proposed work, the surface coverage metric was finally chosen to select the optimal model.

### 2.5. Internode association

An internode is defined as the interval between two consecutive nodes on the same segment. However, TreeQSM performs the reconstruction of each segment at the level of cover sets whose size is usually much smaller than the lengths of internodes. This results in a fact that an internode candidate can be reconstructed by multiple sub-cylinders. To access the phenotypic traits at internode level, the reconstructed sub-cylinders were further allocated into individual internodes, which is known as an internode association process. Potential plant nodes were detected by using the topology and morphology information from the TreeQSM output, i.e. branch morphological order, indices of sub-cylinder candidates within each branch, and parent sub-cylinder indices. Sub-cylinders between two consecutive plant nodes within a segment then form a complete internode candidate.

With a detected internode candidate, internode length was obtained by calculating the distance between the start point of the first sub-cylinder and the terminus of the last sub-cylinder. The diameter of an internode was represented by the mean value of the first and the last sub-cylinder diameters. To obtain the branching angle of a secondary branch, we firstly calculated the orientation vector formed by the start and the terminus points of the petiole. The branching angle was then presented as the angle between the petiole orientation vector and parent stem internode, calculated from Eq. (1):

$$\theta_b = \arccos \left( \frac{\mathbf{O}_1 \mathbf{O}_2}{|\mathbf{O}_1| |\mathbf{O}_2|} \right), \quad (1)$$

where  $\mathbf{O}_1$  and  $\mathbf{O}_2$  refer to orientation vectors of the petiole and the parent stem internode respectively. To obtain the phyllotactic angle of a secondary branch, the petiole orientation vectors of two consecutive branches were projected on a horizontal plane. The angle between these two projected orientation vectors counter-clockwise was calculated as the phyllotactic angle. Here, the phyllotactic angle for the secondary branch at the bottom of a plant was considered as zero. The total length of the stem was then given as the distance between the start point of the bottom sub-cylinder being detected on the stem and the start point of the detected top secondary branch.

### 2.6. Experimental design

The experiment was conducted on a laptop working station with an Intel Xeon E-2276M (2.8 GHz) CPU and a NVIDIA Quadro RTX 5000 Max-Q (16 GB) GPU. The segmentation network was trained over the training set ( $\mathbb{T}_r$ ) containing 35 point clouds for ten times, resulting in ten different segmentation models. The evaluation of the semantic

segmentation result was performed on the test dataset ( $\mathbb{T}_e$ ) containing ten point clouds by using the metrics proposed in Section 2.7. The performance was described by averaging the evaluation results obtained from all these ten segmentation models.

To determine the final segmentation model being used for the phenotyping process, a validation process was employed by using the validation dataset ( $\mathbb{V}$ ) containing five point clouds. The optimal model was selected with the highest stemwork segmentation  $F1$  score. The phenotyping process was then conducted based on the pipeline introduced in Sections 2.3, 2.4, and 2.5. Phenotyping performance was evaluated according to the evaluation metrics described in Section 2.7. To further evaluate the influence of the stemwork segmentation error over the phenotyping performance, a controlled experiment was designed by using the manual segmented stemwork point clouds. The stemwork points were extracted from each point cloud in the test set ( $\mathbb{T}_e$ ) according to the manual annotations. Sub-cylinder models were reconstructed for each stemwork point cloud, followed by the optimal model selection and the internode association. The stemwork point clouds acquired from manual annotations were supposed to be absolutely accurate with satisfactory point densities. Therefore, resampling and noise removal operations were no longer activated in this controlled experiment. The interference branch removal was still employed to remove the bottom side branches which may have negative effects towards the reconstruction. The phenotyping results were then evaluated with the same evaluation metrics, and compared with the evaluation results obtained from the auto-segmented stemwork point clouds.

### 2.7. Evaluation metrics

To evaluate the performance of semantic segmentation, the numbers of True Positives (TP), False Positives (FP), and False Negatives (FN) for respective classes were counted. The segmentation performance of each class was presented by using the metric of  $F1$  score:

$$F1 = \frac{2 * P_r * R_e}{P_r + R_e}, \quad (2)$$

where  $P_r$  refers to the precision calculated from:

$$P_r = \frac{N_{TP}}{N_{TP} + N_{FP}}, \quad (3)$$

and  $R_e$  refers to the recall calculated from:

$$R_e = \frac{N_{TP}}{N_{TP} + N_{FN}}. \quad (4)$$

A  $F1$  score closer to one represents a better segmentation performance.

The evaluation of phenotyping performance was performed for topology and geometry. The topology evaluation aims to assess the coincidence of nodes between the digital plant model and the ground

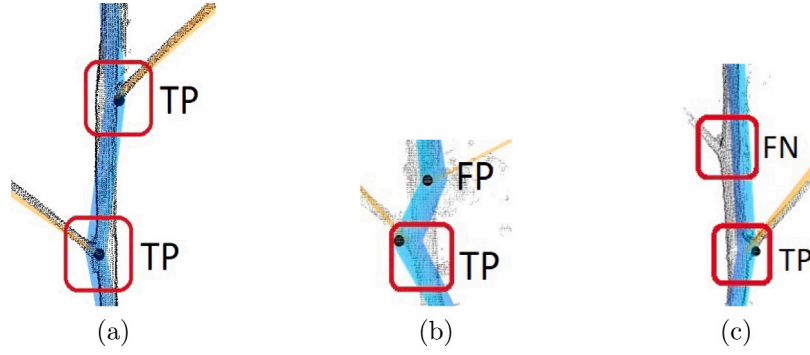


**Fig. 10.** The manual association process of node candidates during the topology evaluation. The ground truth nodes instances are marked by the red rectangular blocks. The node candidates being detected in the digital plant model are marked by black dots. A true positive (TP) candidate refers to a detected node candidate that can be associated with an actual ground truth node instance, as shown in (a), (b) and (c). A false positive (FP) candidate refers to a detected node candidate that cannot be associated with an actual ground truth node instance, as shown in (b). A false negative (FN) candidate refers to a ground truth node that is not detected in the digital plant model, as shown in (c).

truth. The proposed work mainly focused on the evaluation of stem node detection performance because they exerted a significant influence over the calculations of the target phenotypic traits. A feasible way to evaluate the topology reconstruction is to employ the metrics related to the confusion matrix, as proposed in our preceding work (Xin et al., 2020; Xin and Whitty, 2022). The first step is to perform a manual association between the stem nodes in the reconstructed digital plant model and the ground truth point cloud, as shown in Fig. 10. A True Positive (TP) then refers to a node candidate in the digital plant model that is associated with a ground truth node instance. A False Positive (FP) refers to a node candidate in the digital plant model that cannot be associated with a ground truth node instance. A False Negative (FN) refers to a ground truth node instance that cannot be associated with a node candidate in the digital plant model. In this manner, the total numbers of TP, FP, and FN were counted, and the topology reconstruction performance was finally described by the metric of  $P_r$ ,  $R_e$ , and  $F1$  score calculated from Eq. (2). A higher value of  $P_r$ ,  $R_e$ , or  $F1$  refers to a better topology reconstruction performance with more nodes being detected correctly.

The geometry evaluation focused on the accuracy of calculated value of each phenotypic trait, i.e. stem internode length, stem internode diameter, leaf branching angle, leaf phyllotactic angle, and stem length. Due to the scope of the imaging system, certain point clouds within our dataset were not completed at the top part of plants. Therefore, the evaluation on the stem length was only conducted to the visible part of the stem. The performance was presented by Mean Absolute Errors (MAE), related Rooted Mean Squared Errors (rRMSE), and Mean Absolute Percentage Errors (MAPE). The MAE is calculated from Eq. (5):

$$MAE = \frac{1}{N} \sum |\mathbf{v}_c - \mathbf{v}_{gt}|, \quad (5)$$

where  $\mathbf{v}_c$  and  $\mathbf{v}_{gt}$  refer to the calculated phenotypic traits and the corresponding ground truth measurements respectively,  $N$  refers to the number of candidates. The rRMSE is calculated from Eq. (6):

$$rRMSE = \frac{1}{\bar{v}_{gt}} \sqrt{\frac{\sum (\mathbf{v}_c - \mathbf{v}_{gt})^2}{N}} \times 100\%, \quad (6)$$

where  $\bar{v}_{gt}$  stands for the expectation of the ground truth measurements. The MAPE is calculated from Eq. (7):

$$MAPE = \frac{1}{N} \sum \left| \frac{\mathbf{v}_c - \mathbf{v}_{gt}}{\mathbf{v}_{gt}} \right| \times 100\%, \quad (7)$$

It is worthwhile to mention that all the geometry evaluation results were obtained with the true positive candidates only. This is because false positive candidates and false negative candidates cannot be associated with the correct ground truth or reconstructed elements, which

disables the comparison between the calculated phenotypic traits and the corresponding ground truth values.

Within a point cloud of tomato plant, the organs at different morphological ranks have different visibility and organ separability. This exerts uncertainties towards the digital modelling of stemwork and the calculation of phenotypic traits. To further evaluate the influence of organ separability on the performance of phenotyping, the tomato plant was divided into three parts according to the morphological position: (1) morphological top, refers to the top 1/3 morphological ranks in a digital plant model; (2) morphological bottom, refers to the bottom rank being detected in the digital plant model; (3) morphological middle, refers to the middle ranks apart from morphological top and bottom. The performance of plant trait calculations were evaluated with respect to different morphological positions of the plants.

To further investigate the influence of stemwork segmentation performance on the phenotyping result, the distributions of phenotypic traits obtained from different approaches was calculated and presented with histograms. Here, the approaches to acquire phenotyping traits include ground truth measurements, phenotyping from automatic stemwork segmentation, and phenotyping from manual stemwork segmentation (Section 2.6). The similarity among the histograms obtained from the above three approaches was evaluated using the Chi-squared distance:

$$D = 2 \cdot \frac{(\mathbf{h}_1 - \mathbf{h}_2)^2}{\mathbf{h}_1 + \mathbf{h}_2}, \quad (8)$$

where  $\mathbf{h}_1$  and  $\mathbf{h}_2$  refer to the collections of frequencies from two different histograms.

### 3. Results

This section provides the evaluation results for the proposed phenotyping pipeline in aspects of semantic segmentation, stemwork topology reconstruction, and stemwork geometry reconstruction. The segmentation  $F1$  scores for classes of soil base, stick, stemwork and other bio-structures were 0.98, 0.85, 0.65, and 0.96 respectively, resulting in an class-average  $F1$  of 0.86. With respect to the main stem, bottom-rank side branches, middle-rank side branches, and top-rank side branches, the corresponding segmentation  $F1$  scores were 0.92, 0.53, 0.51, and 0.47 respectively. A stemwork segmentation result is visualised in Fig. 11.

The quantitative evaluation result of stemwork topology reconstruction for the auto-segmented and manual-segmented stemwork point clouds are shown in Table 2. The evaluation results for the bottom ranks were not presented. A bottom rank refers to the first morphological rank in a reconstructed digital plant model, which will not have an error when evaluating the topology.

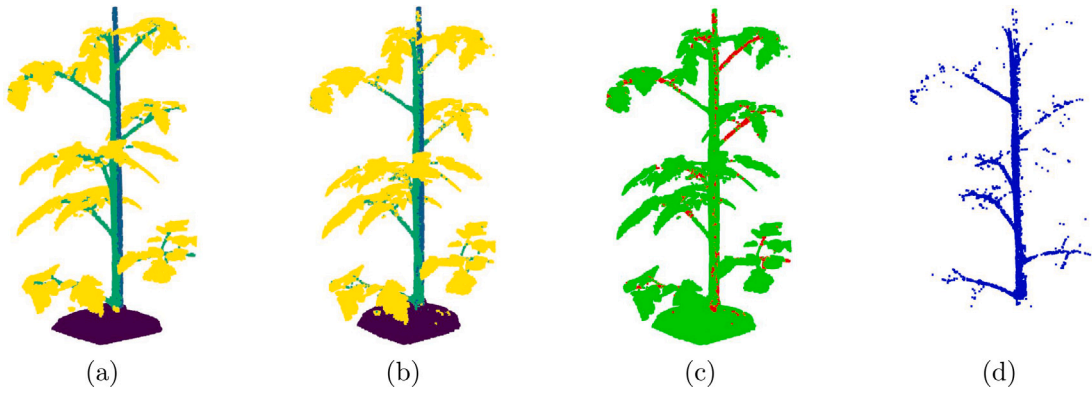


Fig. 11. Plant part semantic segmentation results. (a) shows the ground truth semantic labels; (b) shows the labels predicted by the neuron network; (c) shows the difference between (a) and (b); (d) shows the stemwork extraction result.

**Table 2**  
Evaluation results of topology and geometry reconstruction of the stemwork.

Evaluation types	Stemwork traits	Evaluation metrics	Automatic segmentation				Manual segmentation			
			All	Middle	Bottom	Top	All	Middle	Bottom	Top
Stemwork topology	–	$P_t$	0.89	0.88	–	0.87	1.00	1.0	–	1.0
		$R_c$	0.59	0.91	–	0.30	0.53	0.93	–	0.25
		F1	0.71	0.89	–	0.45	0.69	0.96	–	0.40
Stemwork geometry	Internode length	MAE (mm)	14.2	12.1	12.9	19.7	15.0	12.2	29.4	12.2
		rRMSE (%)	44.8	34.8	29.5	75.5	43.0	29.4	95.4	41.4
		$R^2$	0.71	0.86	0.19	0.52	0.30	0.56	0.02	0.21
	Internode diameter	MAE (mm)	5.2	4.4	3.3	7.9	3.0	2.2	3.6	4.4
		rRMSE (%)	64.4	47.3	31.5	130.0	41.6	24.5	47.9	73.8
		$R^2$	0.04	0.27	0.65	0.02	0.08	0.16	0.00	0.02
	Branching angle	MAE (Degrees)	15.3	9.9	11.9	32.3	12.4	9.4	13.8	17.8
		rRMSE (%)	40.1	23.7	21.0	92.0	33.9	25.7	32.4	52.3
		$R^2$	0.07	0.28	0.79	0.05	0.07	0.04	0.43	0.00
	Phyllotactic angle	MAE (Degrees)	34.5	31.0	–	42.6	34.4	33.3	–	36.7
		rRMSE (%)	28.0	25.5	–	34.7	27.7	27.6	–	27.8
		$R^2$	0.41	0.32	–	0.50	0.17	0.19	–	0.16

In this table, “all”, “middle”, “bottom” and “top” refer to all ranks, middle ranks, bottom rank and top ranks respectively.

In aspects of geometry evaluation, Mean Average Errors (MAE), related Rooted Mean Squared Errors (rRMSE), and  $R$  squares for internode length, internode diameter, branching angle, and phyllotactic angle are presented in Table 2. The MAEs of stem length estimation were calculated as 21.4 and 38.1 mm for the automatic stemwork segmentation and manual segmentation, which results in rRMSEs of 4.8 and 9.3% respectively. The  $R^2$  values for stem length estimation with respect to automatic and manual segmentation were calculated as 0.93 and 0.99. Particularly for internode length, the Mean Absolute Percentage Errors (MAPE) were also calculated using Eq. (7), in order to perform a parallel comparison with the existing work. Corresponding MAPE values for all ranks, the middle ranks, the bottom ranks, and the top ranks were 31.0, 17.4, 75.2, and 32.6% respectively.

The distributions of internode lengths acquired from the ground truth measurements, plant models with automatic segmentation, and plant model with manual segmentation are shown in Fig. 12(a). The Chi-square distance between the ground truth distribution and the automatic segmentation ( $D_{gt}^a$ ) was 66.1; the Chi-square distance between the ground truth distribution and manual segmentation ( $D_{gt}^m$ ) was 80.4; and the Chi-square distance between automatic segmentation and manual segmentation ( $D_a^m$ ) was 32.5. The distributions of internode diameters acquired from the ground truth measurements, the plant model with automatic stemwork segmentation, and the plant model with manual segmentation are shown in Fig. 12(b). The corresponding Chi-square distances of  $D_{gt}^a$ ,  $D_{gt}^m$ , and  $D_a^m$  were 221.1, 222.0, and 63.0 respectively. The distribution of calculated branching angles versus the ground truth is presented in Fig. 12(c). The Chi-square distances of  $D_{gt}^a$ ,  $D_{gt}^m$ , and  $D_a^m$  were 34.2, 24.3, and 30.5 respectively. The distribution of

calculated phyllotactic angles versus the ground truth is presented in Fig. 12(d). The Chi-square distances of  $D_{gt}^a$ ,  $D_{gt}^m$ , and  $D_a^m$  were 46.5, 40.3, and 52.8 respectively.

## 4. Discussion

In this section, a deep analysis of phenotyping result is presented from the aspects of semantic segmentation (Section 4.1), topology reconstruction (Section 4.2), and geometry reconstruction (Section 4.3). Parallel comparisons with existing work on tomato plant phenotyping are also included to reveal the advantages and limitations of the proposed work. Finally, general discussions are provided in Section 4.4.

### 4.1. Semantic segmentation

The stemwork class showed the worst segmentation performance. This is mainly caused by the unbalanced dataset. As shown in Fig. 13, the stemwork class only occupies 10.0% of points within the training set, while the proportion of other bio-structures and soil points sum up to 86.8%. Since the network employed an average cross entropy as the loss function, the classes with the most points exerted a relatively larger influence towards the final loss value than those classes with the least points. This forced the network to pay more attention to the segmentation performance of those classes containing most points during the training. Since this phenomenon commonly exists in the similar types of datasets, future work can be conducted by introducing a class-dependent down sampling strategy (Boogaard et al., 2022) to balance the number of points within each class, from which enhance

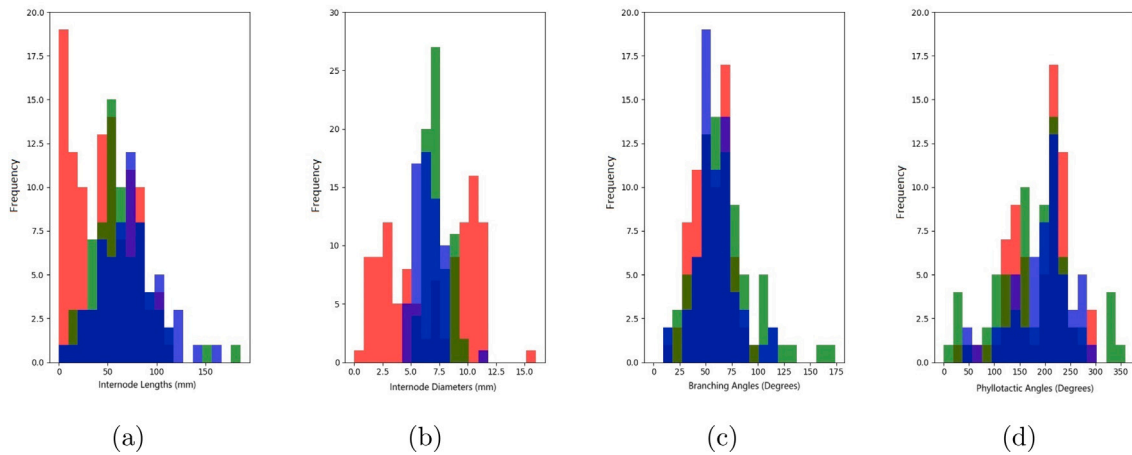


Fig. 12. Distributions of stem internode lengths (a), stem internode diameters (b), branching angles (c), and phyllotactic angles (d) acquired from ground truth measurement (red), automatic segmentation (green), and manual segmentation (blue).

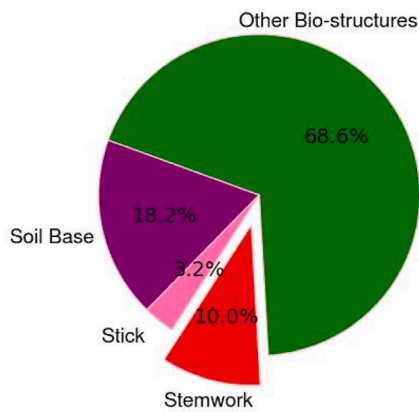


Fig. 13. The proportion of points within the point cloud dataset for respective classes.

the segmentation performance of the stemwork. The performance of the following phenotyping process will directly benefit from the increment of stemwork segmentation accuracy.

Looking at the morphological positions, the top ranks showed the worst stemwork segmentation performance among all. An important reason for this is the poor organ separability close to the morphological top of a plant that gave rise to certain challenges towards the deep neural network. On the other hand, the poor organ separability led to relatively larger subjective errors in the manual annotation compared with other morphological parts, which may also cause certain bias during the evaluation.

#### 4.2. Topology reconstruction

Compared to the performance achieved with the automatic segmentation, the precision achieved with manual segmentation showed higher values. This suggests that the segmentation errors exert certain influence over the topology reconstruction of tomato plant stemwork. For example, certain false positive reconstructions of secondary branches was caused by the segmentation errors between the stick and the stem points. The precision achieved by manual segmentation suggests that the false positive reconstructions can be completely avoided if the stemwork segmentation is accurate enough.

The top ranks achieved a significantly poor recall. Since the sizes of organs close to the morphological top of a plant are usually small, the point cloud resolution – which performed well on the bottom and

the middle ranks – cannot meet the requirement of the top part anymore. As the separability of nodes becomes poorer, the node detection algorithm proposed in Section 2.5 was no longer able to successfully identify the nodes, which resulted in a large number of false negative secondary branches close to the morphological top of plants. Further improvement can be made by employing a dynamic radius when performing the TreeQSM cylinder reconstruction with cover sets. A relatively larger radius can be selected to process the point cloud close to the morphological bottom of the plant to decrease the sensitivity towards the noise, while a smaller radius can be used to process the point cloud with higher morphological ranks in order to capture more details and avoid the false negative reconstructions.

According to the  $F1$  scores, the topology reconstruction at middle ranks achieved a better performance compared to the top ranks. Since TreeQSM pipeline is sensitive towards the quality of stemwork point cloud, this was mainly caused by the relatively lower noise level at middle ranks, giving that the 3D segmentation performance at middle ranks was higher than that at top ranks.

#### 4.3. Geometry reconstruction

Parallel comparison was conducted with respect to four existing work performing 3D phenotyping for tomato plants with both automatic and manual stemwork segmentation approaches (Rose et al., 2015; Rossi et al., 2020, 2022; Wang et al., 2022).

##### 4.3.1. Internode length

The performance presented by the middle-rank candidates indicated relatively smaller rRMSE and larger  $R^2$  values compared to the results of the top ranks. This was mainly a result of the better topology reconstruction performance. For the bottom ranks, a potential factor increasing the internode length estimation errors was the interference branch removal process. The interference branch removal got rid of certain bottom-rank side branches that might cause interference towards the TreeQSM reconstruction (Section 2.3.2). However, the removal of side branches gave rise to false detection of stem nodes. This led to a result that the calculated internode lengths at bottom ranks might be larger than the ground truth values. Future improvement will be conducted by adding a marker at the node where an interference branch is removed, in order to rectify the bias caused by the interference branch removal process. Besides, the limitation of the imaging system also contributed to the fluctuations of the evaluation results at bottom ranks. As mentioned in Section 2.3.2, the stem internodes at bottom ranks might not be completely visible in the point clouds. There might be a part of the internode that was buried in the soil, resulting in certain estimated



internode lengths at bottom ranks to be shorter than the actual values. However, the manual measurement of internode length was performed to the complete internode. This introduced certain systematical errors in the evaluation results. Future work can be conducted to improve the point cloud acquisition mechanism, which provides point clouds with a better visibility at the bottom part. Further, the total number of bottom internode candidates being evaluated was limited, because there is only one bottom stem internode within each plant (Section 2.7). The small number of samples may lead to certain fluctuations towards the evaluation results.

According to Fig. 12(a), the results of internode length calculations with automatic stemwork segmentation and manual stemwork segmentation did not indicate a significant difference. However, both of these results showed large differences compared with the ground truth distribution. This suggested that the digital reconstruction algorithm was potentially responsible for the bias. The topology evaluation showed that there are a large number of false negative candidates close to the morphological top of a plant. This is because a large number of internode candidates were not successfully reconstructed in the digital plant model, which causes the bias of internode length distribution. According to Fig. 12(a), most of the bias in internode length distribution was caused by the internodes with small lengths. Since the internode candidates with top ranks generally have smaller lengths, this provides a further evidence towards the explanation above.

Parallel comparison was performed with an existing work (Wang et al., 2022) whose MAPE of internode length was 20.6%. Since their work employed a manual process to segment the stemwork, the comparison here is based on the internode estimation results with manual stemwork segmentation. The proposed work indicated a better performance in the aspect of middle-rank internode length calculation, while larger errors were observed with respect to top ranks and bottom ranks. This provides a scope for future improvement of the proposed phenotyping pipeline. However, as an automatic phenotyping pipeline, the segmentation error is not avoidable. The performance of their work with the auto-segmentation error is still unknown. Here, we state that the parallel evaluation was performed by directly comparing the evaluation values presented in their article and ours.

#### 4.3.2. Internode diameter

The internode diameter estimation with automatic stemwork segmentation generally resulted in a larger error than the manual stemwork segmentation. The potential segmentation errors gave rise to two effects: (i) the stem internode period is incomplete (false negative); (ii) the points within a stem internode period contain mis-segmented points (false positive) from other classes (soil base, stick, and other bio-structures). Both of the above circumstances led to the incorrect estimations of the fitted cylinder diameters.

The diameter estimation at top ranks showed a larger rRMSE and smaller  $R^2$  compared to other morphological positions. This is caused by the high requirement of surface coverage when performing TreeQSM fitting and the low point density at the morphological top of a plant. On the other hand, the TreeQSM reconstruction algorithm simply employed cylinders to approximate the shape of the stem internodes. However, the actual shape of an stem internode is an irregular elliptical cylinder as mentioned in Section 2.1.2. This may also lead to certain bias in the evaluation results of internode diameters. Future improvement of the model reality and reliability can be achieved by employing elliptical cylinder models to perform the sub-cylinder fitting in the TreeQSM algorithm.

According to Fig. 12(b), the estimated internode diameters indicated much more narrow and concentrated distributions than the ground truth condition. This suggests that the TreeQSM algorithm tends to use medium-size sub-cylinders to fit the stemwork point clouds. The internode diameter distributions from automatic segmentation and manual segmentation did not indicate a significant difference. This further demonstrated that the cylinder fitting algorithm (least square) being

used in TreeQSM might not be perfect, and explains the reason why the diameter estimation indicated low  $R^2$  values with both automatic and manual stemwork segmentation. Future work can focus on selecting a cylinder fitting algorithm with a more robust performance, for example RANdom SAmple Consensus (RANSAC).

#### 4.3.3. Branching angle

The top-rank presented a worse performance comparing with other morphological ranks. This is mainly caused by the worse organ separability at top ranks, giving rise to certain false detection of node positions. A false node detection resulted in an incorrect orientation vector, and consequently a less accurate branching angle. Combined with the segmentation errors, the performance was even worse with the automatic stemwork segmentation from the aspects of MAE and rRMSE. We also noticed that the  $R^2$  values for branching angle estimation were relatively poor. This suggests that the cylinder fitting algorithm being used in the TreeQSM phenotyping pipeline is less accurate in orientation estimation, especially when dealing with noisy and low-resolution point clouds.

According to Fig. 12(c), the distributions of estimated branching angles do not indicate significant differences compared to the ground truth, which shows that the proposed phenotyping pipeline is able to basically describe the variations of branching angles of the tomato plants.

Apart from these, Rossi et al. (2020, 2022) also measured the tomato plant branching angle from 3D point clouds with manual and automatic stemwork segmentation respectively. The definition of branching angle in these research is given by the angle of petiole orientation and the vertical axis (which is also known as zenith angle), which is slightly different from our definition. The rRMSE presented in Rossi et al. (2020, 2022) were 11.2% and 3.7% respectively, which was lower than our rRMSE (33.9% and 40.1% respectively). One of the reasons is that the only factor that influenced the error of branching angles in their research was the accuracy of petiole internode orientation estimation. While in our approach, branching angle refers to the angle between the petiole orientation and the corresponding stem internode orientation. The estimation of the stem internode orientation also introduced certain errors, which explains the relatively larger error for our pipeline. Another important reason giving rise to the difference on phenotyping performance is the quality of the input data. In Rossi et al. (2022), the resolution of input point cloud was 4.88  $\mu\text{m}$ , while in the proposed work, the point cloud resolution was 1 mm instead. The lower resolution of input point cloud led to a worse segmentation performance in our work, whose average segmentation  $F1$  score was 0.86 comparing with 0.97 in their work. As a trade off between accuracy and efficiency, our imaging platform employed a less complex equipment setup, enabling a point cloud reconstruction of target plant within 20  $\mu\text{s}$  (Golbach et al., 2016). This ensures the ability of the proposed pipeline when performing high-throughput plant phenotyping. Besides, the acquisition of ground truth data was different between Rossi et al. (2022) and the proposed work. In Rossi et al. (2022), ground truth measurements were acquired with an existing software - ImageJ. However, considering its limited performance during the complex situations and the potential similarity with the proposed work in aspect of systematic errors, ground truth data was obtained with manual measurements in this paper. Due to the complex structure within the tomato plant canopy, the manual measurements may contain certain subjective errors, especially for the angle measurements. This is also one of the potential reasons leading to the relatively larger errors of branching angle estimation within the proposed work. Here, we state that the parallel evaluation was performed by directly comparing the evaluation values presented in their article and ours.

#### 4.3.4. Phyllotactic angle

A main reason giving rise to the phyllotactic angle estimation errors was the potential subjective errors when performing the manual measurements, considering the difficulties when locating the protractor (Fig. 5) within the dense canopy. This can be partially avoided by averaging the phyllotactic angle measurements from different operators. Another reason was the false positive and false negative node detection results (Section 3), which led to wrong references when calculating the phyllotactic angle for a target secondary branch. Combined with the fact that a poor stemwork segmentation performance may result in a poor topology reconstruction performance (Section 3), this explains why the rRMSE at top ranks with the automatic stemwork segmentation were slightly larger than with the manual segmentation. Since the secondary branches at the bottom rank do not have a reference to calculate the phyllotactic angle, the performance achieved at the bottom rank is not presented.

According to Fig. 12(d), there is no significant difference among the distributions from different source of input, suggesting that the proposed phenotyping pipeline is able to basically describe the variations of phyllotactic angles of the tomato plants.

#### 4.3.5. Stem length

Compared to the rRMSE of stem length estimation presented in Wang et al. (2022) (13.9%), our pipeline achieved a higher accuracy. However, a larger rRMSE was shown compared to Rose et al. (2015) and Rossi et al. (2020, 2022), whose rRMSEs were 1.9, 5.7%, and 3.1% respectively. Due to the limitation on point cloud resolution, the separability of branches at the top part of a plant was commonly poor, which gave rise to a large number of false negatives when performing branch reconstructions at top regions. Since the stem length was presented by the distance between the bottom of stem and the root of top secondary branch, a large number of missing top branches in the digital plant model led to a relatively smaller stem length estimation compared with the ground truth measurement. Here, we state that the parallel evaluation was performed by directly comparing the evaluation values presented in their article and ours.

#### 4.4. General discussion

As introduced in Section 2.4, TreeQSM algorithm requires a parameter proposal process to provide necessary initial values for individual types of parameters. The initialisation process may introduce certain subjective factors that influencing the evaluation result. Besides, the picking of initial values for individual parameters is usually related to the specific morphological traits of the stemwork. Since plants with a same cultivar generally indicated similar topological structure and geometrical parameters, the parameter initialisation process is only required when changing to another cultivars. However, this process may require the operator to have basic knowledge about plant morphology in order to make a better proposal for parameter values, which is considered as a potential limitation of the proposed phenotyping pipeline.

Due to the labour intensive process of manual point cloud annotation and plant traits measurements, the size of the test dataset being used in the proposed work was relatively small. The test samples were consist of four Merlice plants, four Briosio plants, and two Gardener Delight plants. Knowing that the morphology of plant stemwork may possess a large diversity even within a same variety, a small test dataset may give rise to an unbalanced performance during the evaluation process, especially for those statistical evaluation metric (for example,  $R^2$ ). This is also considered as one of the potential limitations of the proposed work.

## 5. Conclusions

3D stemwork phenotyping provides a feasible solution towards the relevant research on plant breeding and crop management. However, Tree Quantitative Structural Modeling (TreeQSM), as a commonly used plant phenotyping pipeline, is sensitive towards the quality of the input stemwork point clouds, which presents a challenge for 3D automatic acquisition of plant phenotypic traits. To provide valid and high-quality inputs for the TreeQSM algorithm, this paper proposed a stemwork refining pipeline containing three main process, i.e. non-replacement resampling, interference branch removal, and noise removal. The proposed 3D tomato plant stemwork phenotyping pipeline enables a fully automatic process in calculating various phenotypic traits at both plant and internode level, even with point cloud data with relatively low resolution and signal-noise ratio. The Mean Absolute Errors (rRMSE) of internode length, internode diameter, leaf branching angle, leaf phyllotactic angle, and stem length range from 4.8 to 64.4%. An important reason giving rise to these errors was the sensitivity towards the noise within the stemwork local reconstruction process. Potential future improvements can be conducted with respect to the following two directions. A learning-based morphology analysis can be employed to replace the existing method in the TreeQSM algorithm, in order to enhance the performance of topology reconstruction. Some other existing work, for instance Accurate-Detailed Tree modelling (ADTree), can also be used to improve the digital reconstruction performance. On the other hand, a further investigation on the potential techniques, for instance transfer learning, to enhance the segmentation performance with limited training data can also be conducted.

#### CRedit authorship contribution statement

**Bolai Xin:** Writing – review & editing, Writing – original draft, Visualization, Software, Methodology, Conceptualization. **Katarína Smoleňová:** Methodology. **Harm Bartholomeus:** Writing – review & editing, Supervision, Methodology, Conceptualization. **Gert Kootstra:** Writing – review & editing, Supervision, Methodology, Conceptualization.

#### Declaration of competing interest

The authors declare that they have no known competing financial interests or personal relationships that could have appeared to influence the work reported in this paper.

#### Acknowledgements

We would like to acknowledge the internal resources from WUR for providing necessary fundings to the relevant research. We would like to give our appreciation to the team of Netherlands Plant Eco-phenotyping Centre (NPEC) for providing the greenhouse to grow the tomato plants used. We dedicate our appreciation to Dr. Rick van Zedde and Dr. Gerwoud Otten in Wageningen University and Research for providing the Maxi-Marvin system to acquire the necessary point cloud dataset. We also give our appreciation to Mr. Akshay Kumar Burusa and Ms. Dide Teeffelen in Wageningen University and Research for their kind assistance in manufacturing the protractor used for the phyllotactic angle measurement.

#### Data availability

Data will be made available on request.

## References

- Altartouri, H., Dua'A, A.M., Idais, A., Tamimi, H., Arafef, R., 2015. Computerized extraction of morphological and geometrical features for plants with compound leaves. URL [https://www.researchgate.net/publication/282002103\\_Computerized\\_Extraction\\_of\\_Morphological\\_and\\_Geometrical\\_Features\\_for\\_Plants\\_with\\_Compound\\_Leaves](https://www.researchgate.net/publication/282002103_Computerized_Extraction_of_Morphological_and_Geometrical_Features_for_Plants_with_Compound_Leaves).
- Andrade-Sanchez, P., Gore, M.A., Heun, J.T., Thorp, K.R., Carmo-Silva, A.E., French, A.N., Salvucci, M.E., White, J.W., 2013. Development and evaluation of a field-based high-throughput phenotyping platform. *Funct. Plant Biol.* 41 (1), 68–79, URL <https://www.publish.csiro.au/fp/Fulltext/FP13126>.
- Bai, G., Ge, Y., Hussain, W., Baenziger, P.S., Graef, G., 2016. A multi-sensor system for high throughput field phenotyping in soybean and wheat breeding. *Comput. Electron. Agric.* 128, 181–192, URL <https://www.sciencedirect.com/science/article/pii/S0168169916302289>.
- Bao, Y., Tang, L., Srinivasan, S., Schnable, P.S., 2019. Field-based architectural traits characterisation of maize plant using time-of-flight 3D imaging. *Biosyst. Eng.* (ISSN: 1537-5110) 178, 86–101. <http://dx.doi.org/10.1016/j.biosystemseng.2018.11.005>, URL <https://www.sciencedirect.com/science/article/pii/S153751101830463X>.
- Boogaard, F.P., Van Henten, E.J., Kootstra, G., 2022. Improved point-cloud segmentation for plant phenotyping through class-dependent sampling of training data to battle class imbalance. *Front. Plant Sci.* 794, URL <https://www.frontiersin.org/articles/10.3389/fpls.2022.838190.full>.
- Boogaard, F.P., van Henten, E.J., Kootstra, G., 2023. The added value of 3D point clouds for digital plant phenotyping – A case study on internode length measurements in cucumber. *Biosyst. Eng.* (ISSN: 1537-5110) 234, 1–12. <http://dx.doi.org/10.1016/j.biosystemseng.2023.08.010>, URL <https://www.sciencedirect.com/science/article/pii/S153751102300171X>.
- Cardellicchio, A., Solimani, F., Dimauro, G., Petrozza, A., Summerer, S., Cellini, F., Renò, V., 2023. Detection of tomato plant phenotyping traits using YOLOv5-based single stage detectors. *Comput. Electron. Agric.* (ISSN: 0168-1699) 207, 107757. <http://dx.doi.org/10.1016/j.compag.2023.107757>, URL <https://www.sciencedirect.com/science/article/pii/S016816992300145X>.
- Diouf, I., Derivot, L., Koussevitzky, S., Carretero, Y., Bitton, F., Moreau, L., Causse, M., 2020. Genetic basis of phenotypic plasticity and genotype × environment interactions in a multi-parental tomato population. *J. Exp. Bot.* (ISSN: 0022-0957) 71 (18), 5365–5376. <http://dx.doi.org/10.1093/jxb/eraa265>, arXiv:<https://academic.oup.com/jxb/article-pdf/71/18/5365/33772291/eraa265.pdf>.
- Du, S., Lindenbergh, R., Ledoux, H., Stoter, J., Nan, L., 2019. AdTree: Accurate, detailed, and automatic modelling of laser-scanned trees. *Remote Sens.* 11 (18), 2074, URL <https://www.mdpi.com/2072-4292/11/18/2074>.
- Fahlgren, N., Gehan, M.A., Baxter, I., 2015. Lights, camera, action: high-throughput plant phenotyping is ready for a close-up. *Curr. Opin. Plant Biol.* (ISSN: 1369-5266) 24, 93–99. <http://dx.doi.org/10.1016/j.pbi.2015.02.006>, URL <https://www.sciencedirect.com/science/article/pii/S1369526615000266>.
- Furbank, R.T., Tester, M., 2011. Phenomics – technologies to relieve the phenotyping bottleneck. *Trends Plant Sci.* (ISSN: 1360-1385) 16 (12), 635–644. <http://dx.doi.org/10.1016/j.tplants.2011.09.005>, URL <https://www.sciencedirect.com/science/article/pii/S1360138511002093>.
- Gehan, M.A., Kellogg, E.A., 2017. High-throughput phenotyping. *Am. J. Bot.* 104 (4), 505–508, URL <https://www.jstor.org/stable/26410949>.
- Golbach, F., Kootstra, G., Damjanovic, S., Otten, G., van de Zedde, R., 2016. Validation of plant part measurements using a 3D reconstruction method suitable for high-throughput seedling phenotyping. *Mach. Vis. Appl.* 27 (5), 663–680, URL <https://link.springer.com/article/10.1007/s00138-015-0727-5>.
- Guo, Y., Wang, H., Hu, Q., Liu, H., Liu, L., Bennamoun, M., 2020. Deep learning for 3D point clouds: A survey. *IEEE Trans. Pattern Anal. Mach. Intell.* URL <https://ieeexplore.ieee.org/abstract/document/9127813>.
- Hang, L., Lie, T., Steven, A. W., Yu, M., 2017. A robotic platform for corn seedling morphological traits characterization. *Sensors* (ISSN: 1424-8220) 17 (9), 2082. <http://dx.doi.org/10.3390/s17092082>, URL <https://www.mdpi.com/1424-8220/17/9/2082>.
- Heiwolt, K., Duckett, T., Cielniak, G., 2021. Deep semantic segmentation of 3D plant point clouds. In: Fox, C., Gao, J., Ghalamzan Esfahani, A., Saaj, M., Hanheide, M., Parsons, S. (Eds.), *Towards Autonomous Robotic Systems*. Springer International Publishing, Cham, pp. 36–45, URL [https://link.springer.com/chapter/10.1007/978-3-030-89177-0\\_4](https://link.springer.com/chapter/10.1007/978-3-030-89177-0_4).
- Itakura, K., Hosoi, F., 2018. Automatic leaf segmentation for Estimating Leaf Area and leaf inclination angle in 3D plant images. *Sensors* (ISSN: 1424-8220) 18 (10), <http://dx.doi.org/10.3390/s18103576>, URL <https://www.mdpi.com/1424-8220/18/10/3576>.
- Laxman, R., Hemamalini, P., Bhatt, R., Sadashiva, A., 2018. Non-invasive quantification of tomato (*Solanum lycopersicum* L.) plant biomass through digital imaging using phenomics platform. *Indian J. Plant Physiol.* 23, 369–375, URL <https://link.springer.com/article/10.1007/s40502-018-0374-8>.
- Li, S., Dai, L., Wang, H., Wang, Y., He, Z., Lin, S., 2017. Estimating Leaf Area density of individual trees using the point cloud segmentation of terrestrial LiDAR data and a voxel-based model. *Remote Sens.* (ISSN: 2072-4292) 9 (11), <http://dx.doi.org/10.3390/rs9111202>, URL <https://www.mdpi.com/2072-4292/9/11/1202>.
- Li, Z., Guo, R., Li, M., Chen, Y., Li, G., 2020. A review of computer vision technologies for plant phenotyping. *Comput. Electron. Agric.* (ISSN: 0168-1699) 176, 105672. <http://dx.doi.org/10.1016/j.compag.2020.105672>, URL <https://www.sciencedirect.com/science/article/pii/S0168169920307511>.
- Li, L., Zhang, Q., Huang, D., 2014. A review of imaging techniques for plant phenotyping. *Sensors* (ISSN: 1424-8220) 14 (11), 20078–20111, URL <https://www.mdpi.com/1424-8220/14/11/20078>.
- Mahlein, A.-K., 2016. Plant disease detection by imaging sensors-parallel and specific demands for precision agriculture and plant phenotyping. *Plant Dis.* 100 (2), 241–251, URL <https://apsjournals.apsnet.org/doi/full/10.1094/PDIS-03-15-0340-FE>.
- Paul, K., Sorrentino, M., Lucini, L., Roupael, Y., Cardarelli, M., Bonini, P., Reynaud, H., Canaguier, R., Trtlele, M., Panzarová, K., Colla, G., 2019. Understanding the biostimulant action of vegetal-derived protein hydrolysates by high-throughput plant phenotyping and metabolomics: A case study on tomato. *Front. Plant Sci.* (ISSN: 1664-462X) 10, 47. <http://dx.doi.org/10.3389/fpls.2019.00047>, URL <https://www.frontiersin.org/article/10.3389/fpls.2019.00047>.
- Phillips, R.L., 2010. Mobilizing science to break yield barriers. *Crop Sci.* 50, S–99, URL <https://access.onlinelibrary.wiley.com/doi/full/10.2135/cropsci2009.09.0525>.
- Qi, C.R., Su, H., Mo, K., Guibas, L.J., 2017a. Pointnet: Deep learning on point sets for 3d classification and segmentation. In: *Proceedings of the IEEE Conference on Computer Vision and Pattern Recognition*. pp. 652–660, URL [https://openaccess.thecvf.com/content\\_cvpr\\_2017/html/Qi\\_PointNet\\_Deep\\_Learning\\_CVPR\\_2017\\_paper.html](https://openaccess.thecvf.com/content_cvpr_2017/html/Qi_PointNet_Deep_Learning_CVPR_2017_paper.html).
- Qi, C.R., Yi, L., Su, H., Guibas, L.J., 2017b. Pointnet++: Deep hierarchical feature learning on point sets in a metric space. *arXiv preprint URL https://proceedings.neurips.cc/paper/2017/hash/d8bf84be3800d12f74d8b05e9b89836f-Abstract.html*.
- Raunonen, P., 2015. Instructions for MATLAB-software TreeQSM, version 2.4.1. In: *Mathematics*. Tampere University, URL [https://github.com/InverseTampere/TreeQSM/blob/master/Manual/TreeQSM\\_documentation.pdf](https://github.com/InverseTampere/TreeQSM/blob/master/Manual/TreeQSM_documentation.pdf).
- Raunonen, P., Kaasalainen, M., Åkerblom, M., Kaasalainen, S., Kaartinen, H., Vastaranta, M., Holopainen, M., Disney, M., Lewis, P., 2013. Fast automatic precision tree models from terrestrial laser scanner data. *Remote Sens.* (ISSN: 2072-4292) 5 (2), 491–520. <http://dx.doi.org/10.3390/rs5020491>, URL <https://www.mdpi.com/2072-4292/5/2/491>.
- Rose, J.C., Paulus, S., Kuhlmann, H., 2015. Accuracy analysis of a multi-view stereo approach for phenotyping of tomato plants at the organ level. *Sensors* (ISSN: 1424-8220) 15 (5), 9651–9665. <http://dx.doi.org/10.3390/s150509651>, URL <https://www.mdpi.com/1424-8220/15/5/9651>.
- Rossi, R., Costafreda-Aumedes, C.L.S., Leolini, L., Bindi, M., Zaldei, A., Moriondo, M., 2020. Performances evaluation of a low-cost platform for high-resolution plant phenotyping. *Sensors* 20 (11), 3150, URL <https://www.mdpi.com/1424-8220/20/11/3150>.
- Rossi, R., Costafreda-Aumedes, S., Leolini, L., Leolini, C., Bindi, M., Moriondo, M., 2022. Implementation of an algorithm for automated phenotyping through plant 3D-modeling: A practical application on the early detection of water stress. *Comput. Electron. Agric.* (ISSN: 0168-1699) 197, 106937. <http://dx.doi.org/10.1016/j.compag.2022.106937>, URL <https://www.sciencedirect.com/science/article/pii/S016816992200254X>.
- Sarlikioti, V., de Visser, P.H.B., Buck-Sorlin, G.H., Marcelis, L.F.M., 2011a. How plant architecture affects light absorption and photosynthesis in tomato: towards an ideotype for plant architecture using a functional-structural plant model. *Ann. Botany* 108 (6), 1065–1073, URL <https://doi.org/10.1093/aob/mcr221>.
- Sarlikioti, V., de Visser, P.H.B., Marcelis, L.F.M., 2011b. Exploring the spatial distribution of light interception and photosynthesis of canopies by means of a functional-structural plant model. *Ann. Botany* 107 (5), 875–883, URL <https://doi.org/10.1093/aob/mcr006>.
- Schunck, D., Magistri, F., Rosu, R.A., Corneliu en, A., Chebrolu, N., Paulus, S., Léon, J., Behnke, S., Stachniss, C., Kuhlmann, H., Klingbeil, L., 2021. Pheno4D: A spatio-temporal dataset of maize and tomato plant point clouds for phenotyping and advanced plant analysis. *PLoS One* 16, 1–18. <http://dx.doi.org/10.1371/journal.pone.0256340>.
- Sheikh, M., Iqra, F., Ambreen, H., Pravin, K.A., Ikra, M., Chung, Y.S., 2024. Integrating artificial intelligence and high-throughput phenotyping for crop improvement. *J. Integr. Agric.* (ISSN: 2095-3119) 23 (6), 1787–1802. <http://dx.doi.org/10.1016/j.jia.2023.10.019>, URL <https://www.sciencedirect.com/science/article/pii/S2095311923003611>.
- Wang, Y., Hu, S., Ren, H., Yang, W., Zhai, R., 2022. 3DphenoMVS: A low-cost 3D tomato phenotyping pipeline using 3D reconstruction point cloud based on multiview images. *Agronomy* 12 (8), 1865, URL <https://www.mdpi.com/2073-4395/12/8/1865>.
- Wu, S., Wen, W., Xiao, B., Guo, X., Du, J., Wang, C., Wang, Y., 2019. An accurate skeleton extraction approach from 3D point clouds of maize plants. *Front. Plant Sci.* (ISSN: 1664-462X) 10, 248. <http://dx.doi.org/10.3389/fpls.2019.00248>, URL <https://www.frontiersin.org/article/10.3389/fpls.2019.00248>.
- Xiang, L., Bao, Y., Tang, L., Ortiz, D., Salas-Fernandez, M.G., 2019. Automated morphological traits extraction for sorghum plants via 3D point cloud data analysis. *Comput. Electron. Agric.* (ISSN: 0168-1699) 162, 951–961. <http://dx.doi.org/10.1016/j.compag.2019.05.043>, URL <https://www.sciencedirect.com/science/article/pii/S0168169919301462>.

- Xin, B., Ji, S., Harm, B., Gert, K., 2023. A 3D grape bunch reconstruction pipeline based on constraint-based optimisation and restricted reconstruction grammar. *Front. Plant Sci.*
- Xin, B., Liu, S., Whitty, M., 2020. Three-dimensional reconstruction of vitis vinifera (L.) cvs Pinot Noir and Merlot grape bunch frameworks using a restricted reconstruction grammar based on the stochastic L-system. *Aust. J. Grape Wine Res.* 26 (3), 207–219, URL <https://onlinelibrary.wiley.com/doi/full/10.1111/ajgw.12444>.
- Xin, B., Whitty, M., 2022. A 3D grape bunch reconstruction pipeline based on constraint-based optimisation and restricted reconstruction grammar. *Comput. Electron. Agric.* 196, 106840, URL <https://www.sciencedirect.com/science/article/pii/S0168169922001570>.
- Zhang, Y., Teng, P., Aono, M., Shimizu, Y., Hosoi, F., Omasa, K., 2018. 3D monitoring for plant growth parameters in field with a single camera by multi-view approach. *J. Agric. Meteorol.* 74 (4), 129–139, URL [https://www.jstage.jst.go.jp/article/agrmet/74/4/74\\_D-18-00013/\\_article](https://www.jstage.jst.go.jp/article/agrmet/74/4/74_D-18-00013/_article).
- Zhu, T., Ma, X., Guan, H., Wu, X., Wang, F., Yang, C., Jiang, Q., 2023. A calculation method of phenotypic traits based on three-dimensional reconstruction of tomato canopy. *Comput. Electron. Agric.* (ISSN: 0168-1699) 204, 107515. <http://dx.doi.org/10.1016/j.compag.2022.107515>, URL <https://www.sciencedirect.com/science/article/pii/S0168169922008237>.
- Ziamtsova, I., Navlakha, S., 2019. Machine learning approaches to improve three basic plant phenotyping tasks using three-dimensional point clouds. *Plant Physiol.* 181 (4), 1425–1440, URL <https://academic.oup.com/plphys/article/181/4/1425/6000535>.